Evaluating Mesoscale Simulations of the Coastal Flow Using Lidar Measurements

Floors, Rogier Ralph; Hahmann, Andrea N.; Pena Diaz, Alfredo

Published in:
Journal of Geophysical Research: Atmospheres

Link to article, DOI:
10.1002/2017JD027504

Publication date:
2018

Document Version
Early version, also known as pre-print

Evaluating mesoscale simulations of the coastal flow using lidar measurements

R. Floors[1], A.N. Hahmann[1] and A. Peña[1]

[1]DTU Wind Energy, Technical University of Denmark, Roskilde, Denmark

Key Points:

- Sensitivity study of the WRF model setup to boundary-layer scheme, atmospheric boundary conditions, surface description, sea surface temperatures and horizontal resolution
- First time that a mesoscale model is evaluated with horizontal transects across the coast using lidar measurements.
- Studies the processes that govern the flow in the coastal zone during a 3 month period.

Corresponding author: Rogier Floors, `rofl@dtu.dk`

Abstract

The atmospheric flow in the coastal zone is investigated using lidars, mast measurements and model simulations. The Weather, Research and Forecasting (WRF) model is set-up in 12 different configurations using 2 planetary boundary-layer schemes, 3 horizontal grid spacings and varied sources of land use, and initial and lower boundary conditions. All model simulations describe the observed mean wind profile well at different onshore and offshore locations from the surface up to 500 m. The simulated mean horizontal wind speed gradient across the shoreline is close to that observed, although all simulations show wind speeds that are slightly higher than those observed. Inland at the lowest observed height, the model has the largest deviations compared to the observations. Taylor diagrams show that using ERA-interim data as boundary conditions improves the model skill scores. Simulations with the finest horizontal grid show poorer model performance. Modelled and observed spectra were compared and showed that, although having a negative impact on standard performance metrics, simulations with the finest horizontal grid spacing resolved more high-frequency atmospheric motion.The results show that to describe and understand the flow over the coast and the simulations for the WRF model, lidar measurements are of great value.

1 Introduction

There is strong interest in accurate estimation of the wind resource for wind farms that are located in the coastal zone. These areas, defined here as approximately within 10 km of the coastline, have high wind speeds for onshore flow conditions, grid connectivity is relatively easy and requires little additional investment compared to offshore projects. *Barthelmie et al.* [2007] showed that the flow at a distance less than 20 km from the coastline is not in equilibrium with the new surface conditions and to capture the transition, a model is required.

Due to increasing computing power, it has become popular to use the output from mesoscale models to determine the wind resource [*Frank et al.*, 2001; *Dvorak et al.*, 2009; *Tammelin et al.*, 2013]. Mesoscale models are particularly useful for offshore wind resource estimation, due to the absence of complex and unresolved microscale features [*Dvorak et al.*, 2009; *Wijnant et al.*, 2014; *Hahmann et al.*, 2015]. At Fino3 in the North Sea, an inter-comparison of 26 model simulations showed a mean bias of less than 0.25 $\mathrm{m\,s^{-1}}$ at 90 m [*Olsen et al.*, 2017]. Near the coast, mesoscale models have difficulties in correctly simulating the atmospheric flow due to the influence of surface roughness changes [*Floors et al.*, 2013], coastal

low-level jets (LLJs) [*Hunt et al.*, 2004] and wave-atmosphere interactions [*Lange et al.*, 2004].

The Weather Research and Forecasting (WRF) mesoscale model is frequently used to simulate mesoscale flows [*Skamarock et al.*, 2008]. *Dörenkämper et al.* [2015] used WRF model simulations with a horizontal grid spacing of 700 m to show that streaks of lower wind speed resulting from patches of land with higher surface roughness, can extent several tens of kilometers from the coast during offshore flow. *Floors et al.* [2013] used the WRF model to investigate the impact of vertical resolution and found that it had a negligible impact on the wind profile at one of the locations studied in this paper. Nocturnal LLJs were observed for easterly winds, resulting from cooling of the surface and decoupling of the flow. For westerly winds, the model strongly underestimated the wind speed, which raised the question whether mesoscale models can accurately simulate the flow in the coastal zone.

A correct description of all boundary conditions is necessary to simulate the flow in the coastal zone. The impact of changing the model grid spacing, the description of sea surface temperature (SST), land cover and atmospheric boundary conditions on the simulated wind speed in the coastal zone for an extended period has not been described extensively in literature. Here we investigate such impacts by using two types of land cover data, two sources of SSTs and two sources of atmospheric (re)analysis data.

The large changes in surface roughness and stability and the resulting internal boundary layers are often not resolved at grid spacings of $\approx$ 1 km of the current generation of mesoscale models. Still, Planetary Boundary Layer (PBL) schemes are increasingly being used at very high resolutions, where turbulent motions are partially resolved [*Shin and Dudhia*, 2016]. With the increase in computer power, this trend will continue. To understand better the behaviour of the WRF model and the different PBL schemes at these high resolutions, it is important that the model is evaluated against high-quality measurements.

Wind lidars measure the wind accurately and are now widely used for research and industrial applications [*Mikkelsen*, 2014]. They are usually configured to measure at a number of heights to retrieve the vertical profile of wind speed. Recently, scanning lidars with a steerable scanner head have been developed that are able to point in any direction [*Vasiljević et al.*, 2016].

In this study, our goal is to use the scanning lidar measurements to document the sensitivity of the WRF model to different setups by investigating vertical profiles, horizontal transects, a combination of all measurements and velocity spectra. The vertical profile of wind speed is determined by the representation of turbulent mixing processes over surfaces with different roughness and stability conditions. The horizontal transects show the model's ability to capture changes in surface roughness resulting from the coastline. All measurements can be combined to compute different error metrics and to identify which setup performs the best. Finally, the impact of the model horizontal resolution is studied using modelled and observed velocity spectra.

In Sect. 2 we describe the measurements and the experimental site. Details about the modelling setup and a description of the different sensitivity experiments are given in Sect. 3. In Sect. 4.1 we evaluate the simulated vertical profile of mean wind speed at different locations and in Sect. 4.2 we compare the simulated mean horizontal wind speed gradient across the coast with the scanning lidar measurements. In Sect. 4.3, Taylor diagrams are used to provide an overview of the performance of the different model setups. Finally, we study modelled and observed velocity spectra in Sect. 4.4.

2 Measurements

We use measurements from lidars and a mast and the positions of all instruments are given in Fig. 1a and Table 1. The instruments and measurements are described in detail in *Floors et al.* [2016]. The data used in this paper are available for download [*Floors et al.*, 2017].

The terrain of the experimental area is characterized by grass and crop fields with scattered houses and vegetation. The topography around the site is dominated by a steep cliff at the coast, whereas the terrain is undulating inland (see Fig. 1a). To the north of the area, near position 3, the height of the cliff is $\approx$ 40 m, near position 2 $\approx$ 25 m and near position 1 it becomes a dike of $\approx$ 15 m.

2.1 Vertical profiling lidars

The vertically profiling lidars WLS66 and Alizé were operating at position 2. Bura and 3E were installed $\approx$ 1 km and 400 m inland at positions 5 and 4, respectively. Another vertical profiling lidar was mounted on a buoy at position 6, $\approx$8 km offshore. Due to high waves

during a storm the power generator was damaged and therefore the lidar stopped working on the 7th of December. Due to bad weather and logistical issues, it was not possible to repair the power generator before 11 February. To avoid the influence of breaking waves, the buoy was moved to position 7.

The profiling lidars were configured to perform scans in a Velocity Azimuth Display (VAD) mode, i.e the wind vector was reconstructed from four points separated 90° around the zenith. Data higher than 130 m and with a carrier-to-noise ratio (CNR) lower than −22 dB were filtered out. A limit of −32 dB is used for Alizé, because it is a long-range lidar with a stronger laser. This can measure up to 2000 m height [*Gryning et al.*, 2016]. These limits were chosen to increase the correlation between the wind speeds obtained from the lidars with those observed at the meteorological mast [*Floors et al.*, 2016].

For each of the lidars, the recovery rate is shown in Table 1, which is defined as the percentage of data that fulfilled the filtering criteria divided by the 17281 10-min periods covering the whole campaign that started on 2 November 2015 and lasted until 1 March 2016. Note that Alizé and Bura did not start measuring before 9 and 12 of November, respectively, which partially explains the lower recovery percentage compared to the mast (position 8 in Fig. 1). The lidar buoy recovery rate is much lower than that of the other lidars due to the technical problems and its measurements are split over the two locations.

2.2 Scanning lidars

The scanning lidars are modified versions of the WindCube 200S from the company Leosphere and have been successfully used in several field campaigns [*Vasiljević et al.*, 2016]. They were placed on top of the cliff to have an unobstructed line-of-sight. Different scanning patterns were configured during the experiment, but in this study we only use the measurements obtained between 26 November and 17 February [*Floors et al.*, 2016]. Two spatially separated scanning lidars can estimate the horizontal wind speed vector from measurements of the line-of-sight velocity assuming a zero vertical wind speed. The lidars Koshava and Sterenn used this ‘dual setup’ to scan three virtual horizontal lines at 50, 100 and 150 m above mean sea level (amsl) from $\approx$ 5 km offshore up to $\approx$ 4 km inland (Fig. 2). The lidar Vara performed a plan position indicator (PPI) scan or sector-scan setup (Fig. 2); it scanned 60° of an azimuthal plane up to $\approx$ 8 km distance. This plane was sampled at three different elevation angles, such that these planes approximately intersected with the height of the three

dual setup sampling points $\approx$ 5 km offshore at 50, 100 and 150 m amsl. Both the dual and sector-scan setup performed a full scan in ≈145 s. The available samples of the wind speed components were than averaged in periods of 10 min.

The availability of the scanning lidars is lower than that of the lidars in VAD mode because of the long distance to the sampling point. Similarly to the profiling lidars, we require measurements in all range gates to fulfill a CNR threshold. For the dual setup, the CNR limit was −26.5 dB, whereas for the lidar in sector-scan mode it was −27 dB. Finally, the measurements from the sector-scan and the dual setup are merged with those from the vertical profiling lidars and the mast. The lidar beam hitted objects in the eastward direction after ≈2 km and therefore transects in the range from 5000 m west to 2000 m east of Vara were used. Sampling points from the dual setup between $x = 445615$ and 446215 m (UTM WGS84, zone 32V) were removed because uncertainty in reconstruction of the wind speed is too large when the angle between the line of sights is more than $\approx 160^\circ$. After filtering, 731 10-min transects remained, i.e a recovery rate of 4.23%.

2.3 Meteorological mast

The Høvsøre meteorological mast is located ≈6 km south and ≈2 km inland of Vara (position 8 in Fig.1a). The measurements performed at this mast are thoroughly quality controlled [*Peña et al.*, 2016]. We use the 10-min mean wind speeds obtained with Risø cup anemometers at the southern side of the mast at 10, 40, 60, 80, 100 and 160 m. Horizontal velocity spectra were computed from the cup anemometer at 100 m height. The measuring frequency of the cup anemometer is 10 Hz, but here we are only interested in mesoscale fluctuations and therefore the measurements were down-sampled to 0.1 Hz. The measurements were linearly interpolated to fill missing data in the 0.1 Hz time series. A fast-Fourier transform was performed on linearly detrended ≈14 day periods (2^{11} 10-min periods).

3 Mesoscale modeling

3.1 Basic setup

We use the WRF model to perform simulations during the measurement period. We used version 3.6, to which patches and bug fixes were applied [*Skamarock et al.*, 2008; WRF, 2015]. There were 70 vertical model levels, with its highest density near the surface. The WRF model top was set at 50 hPa. The first model level was at 11 m above the surface and

Table 1. Positions, names, types, main scanning strategies (usage) and coordinates (UTM WGS84, Zone 32V) of the lidars during the RUNE campaign (see details in the text), including the information of the Høvsøre meteorological mast. *N* denotes the number of 10-min mean observations and the recovery percentage is given as a percentage of the total number of attainable 10-min intervals. The lidar buoy was used at two positions. The type is the commercial name given by the lidar manufacturer Leosphere

Pos.	Name	Type	Usage	Easting (m)	Northing (m)	Height amsl (m)	N	Recovery [%]
1	Koshava	WLS200S-007	Dual setup	446080.03	6259660.30	12.36	713	4.23
2	Vara	WLS200S-012	Sector scan	445915.64	6261837.49	26.38	713	4.23
2	Alizé	WLS70-001	Vertical Profile	445915.64	6261837.49	26.38	9866	57.09
2	WLS66	WLS7-066	Vertical Profile	445915.64	6261837.49	26.38	9866	57.09
3	Sterenn	WLS200S-006	Dual setup	445823.66	6263507.90	42.97	713	4.23
4	3E	WLS7-007	Vertical Profile	446379.30	6263251.46	43.18	13580	78.58
5	Bura	WLS7-002	Vertical Profile	447040.74	6263273.41	24.93	10910	63.13
6	Lidar Buoy Pos1	WLS7-277	Vertical Profile	438441	6262178	0.00	3859	22.33
7	Lidar Buoy Pos2	WLS7-277	Vertical Profile	440616	6262085	0.00	1375	7.96
8	Høvsøre mast	-	Mast	447642	6255431	0.32	16383	94.80

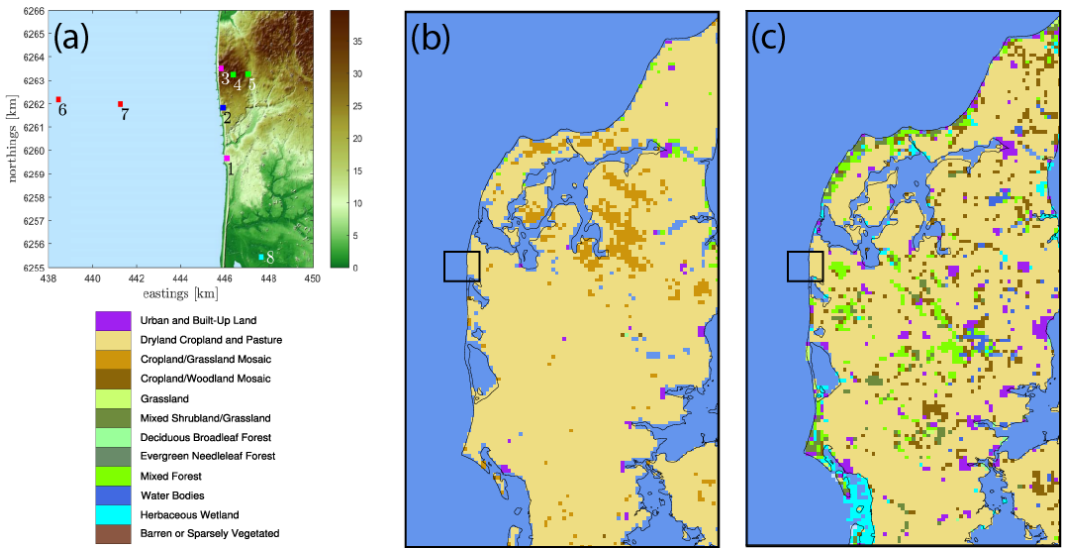

Figure 1. (a). Terrain height (in m) and the positions of the instruments denoted with numbered points (Table 1). The vertically profiling lidars WLS66 and Alizé are collocated with Vara in position 2. Land use description from the model simulations obtained from the (b) USGS and (c) CORINE data set . The area of panel (a) is denoted with a black rectangle.

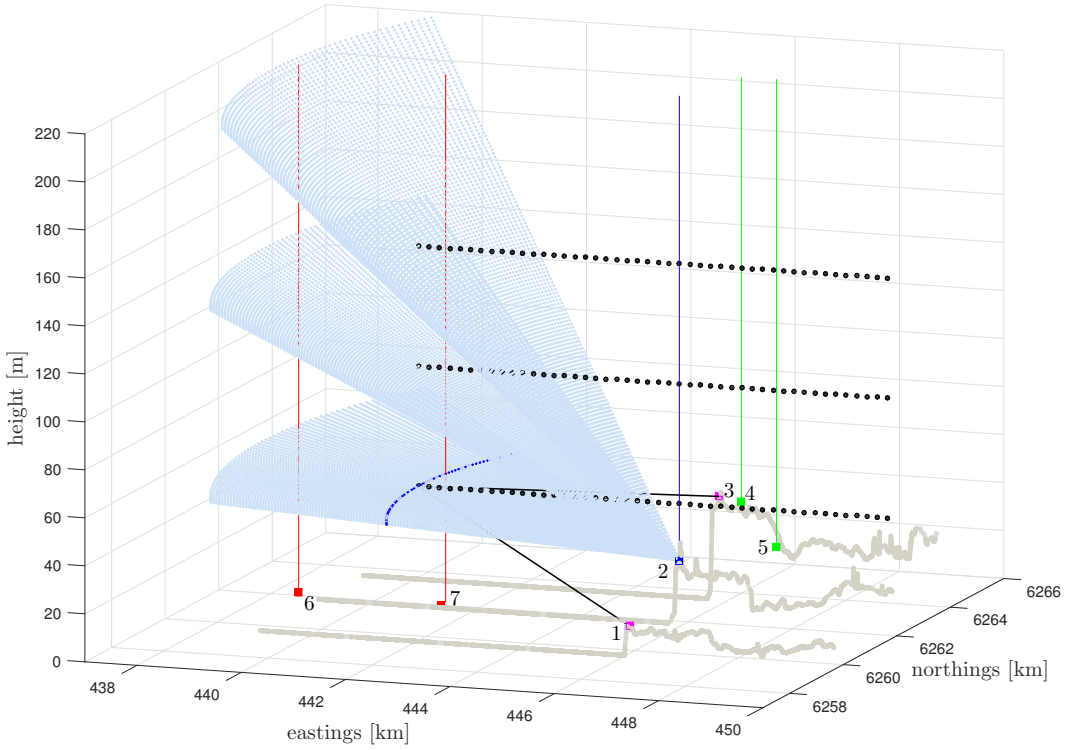

Figure 2. Overview of the main scanning patterns during the measurement campaign. The light blue points denote the sector scan from Vara, the black dots denote the collocated range gates from Sterenn and Koshava, the green lines denote the lidars 3E and Bura, the blue line denotes the lidars WLS66 and Alizé and the red line denotes the lidar buoy in its second position. The dark blue points from the sector scan denote an arch from which the wind vector can be reconstructed.

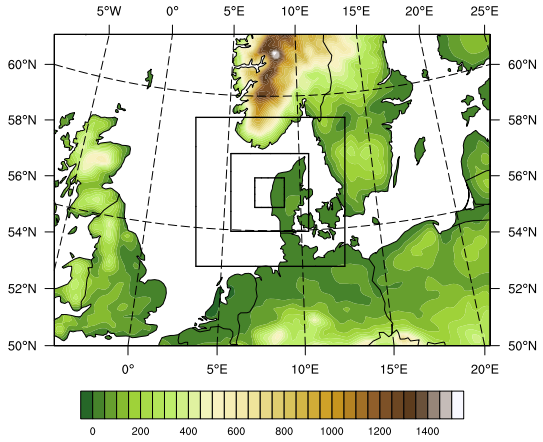

Figure 3. Surface elevation (m) of the outer model domain with the location of three nested model domains indicated.

there were 8 model levels within the first 100 m. The model domains are shown in Fig. 3 and cover a large part of northwestern Europe. One-way nested domains were used to obtain a high horizontal resolution near the experimental site, with a grid-spacing ratio of three between the parent and child nests. The domain boundaries were chosen such that they were at approximately the same geographical location for all setups with different horizontal grid spacings.

The simulations were initialized everyday at 0000 UTC and were integrated for 36 hours. The first 12 hours were disregarded as model spin-up period. The instantaneous output of the model was saved every 10 min for the third and fourth nested domains and hourly for the other domains. The model time step was 65.45 s in the outermost domain and decreased with the same factor as the model grid spacing for the nested domains. Spectral nudging was used above the 25th model level ($\approx$ 600 m) to avoid that the model drifts too much from the large-scale synoptic conditions. The nudging coefficient was set to 0.0003 s^{-1} for wind, temperature and specific humidity, and it was always set to zero at model levels lower than the PBL height.

The physical parametrizations options included the WRF single-moment 5-class micro physics scheme, the Kain-Fritsch cumulus parameterization (turned off in domain three and four), the RRTMG scheme for short and long-wave radiation and the Noah land surface model.

The wind speeds were obtained from the lowest 34 model levels and vertically logarithmically interpolated to the heights of the observations. Horizontally, the grid point closest to the positions where observations were available were extracted.

3.2 Sensitivity studies

The following model sensitivity studies were performed to investigate the impact on the model performance in the experimental area.

3.2.1 PBL scheme

The first-order Yonsei University (YSU) and the 1.5-order Mellow-Yamada Janjic (MYJ) closure schemes were used to represent the PBL [*Noh et al.*, 2003; *Janjić*, 1990] (see Table 2). All sensitivity set-ups introduced further on were performed with both PBL schemes.

3.2.2 Horizontal grid spacing

Three different horizontal grid spacings were used. The first set-up has a spacing of 18, 6 and 2 km for the outermost, middle and innermost domain, respectively. The second set-up uses 9, 3 and 1 km in those domains and the finest spacing used four nested domains with a spacing of 13.5, 4.5, 1.5 and 0.5 km. The resolution of the innermost domain is used as a subscript in Table 2. Despite the relatively high resolution, there is still a difference of $\approx$ 20 m between the observed terrain elevation and that used as input for the simulations with the finest horizontal grid spacing at the position of the cliff. That is partly because the resolution is insufficient in the elevation data itself (see Sect. 3.2.3), but mostly because the WRF model needs input data that is interpolated to the coarser model grid.

Wyngaard [2004] introduced the concept of modelling in the 'terra incognita', i.e. when the scale of the spatial filter of a mesoscale model is similar to the dominant length scale of the flow. For a convective boundary-layer, this characteristic scale is about 1 km and therefore some of our simulations can partially resolve turbulence. However, the PBL schemes in a mesoscale model are developed under the assumption that all turbulent motions are in the subgrid-scale. Because the RUNE experiment took place during winter, stable and neutral conditions prevail and the turbulent eddies are expected to be smaller than in unstable conditions. On the other hand, cold-air advection over a warm North Sea can still result in

Table 2. Abbreviated name, the atmospheric boundary conditions, PBL scheme, SST source, land-cover source and the horizontal resolution of the innermost domain of the modelling set-ups used during the RUNE campaign.

Model Simulation	Atmos. Bound. cond.	PBL scheme	SST source	land cover source	horizontal grid spacing [m]
YSU_2	FNL	YSU	DMI	CORINE	2000
YSU_1	FNL	YSU	DMI	CORINE	1000
$YSU_{0.5}$	FNL	YSU	DMI	CORINE	500
MYJ_2	FNL	MYJ	DMI	CORINE	2000
MYJ_1	FNL	MYJ	DMI	CORINE	1000
$MYJ_{0.5}$	FNL	MYJ	DMI	CORINE	500
YSU_{HRSST}	FNL	YSU	HR	CORINE	2000
MYJ_{HRSST}	FNL	MYJ	HR	CORINE	2000
YSU_{USGS}	FNL	YSU	DMI	USGS	2000
MYJ_{USGS}	FNL	MYJ	DMI	USGS	2000
YSU_{ERA}	ERA	YSU	DMI	CORINE	2000
MYJ_{ERA}	ERA	MYJ	DMI	CORINE	2000

unstable boundary layers; during 15% of the time of the campaign the modelled PBL height at position 7 was more than 1000 m.

3.2.3 Terrain elevation and land use

The description of the land cover is important to correctly assign the surface albedo, the emissivity and the roughness length to the land around the experimental area. In this study, the land-use is also vital for correctly positioning the coastline. The standard land-use description that is often used with the WRF model is based on the 24-category United States Geological Survey (USGS) data [*Anderson et al.*, 1976]. However, it is a rather outdated data

set that represents the land-use conditions in 1992 [*Nielsen*, 2013]. In the USGS data set the main land use in Denmark is cropland, with very few forests and built-up areas (Fig. 1b).

A more recent attempt to describe the land-use in Europe was made as part of the CORINE project. The resulting data set is freely available online [COR, 2006]. The version used here reflects the land-use situation in 2006 and has a grid spacing of 250 m. The CORINE data are divided in 44 categories, but these were reassigned to the same 24 categories as the USGS data [*Pindea et al.*, 2002]. In the CORINE data set, Denmark has many scattered villages and forests, which is more realistic than the rather homogeneous landscape in the USGS data (see Fig. 1b and 1c).

A 25th landuse category is reserved for describing lakes. This can be important in Denmark, because inland water bodies can freeze during winter and can therefore have a water temperature that is very different from that of the North Sea. The water temperature from a lake in WRF is estimated from the averaged soil temperature in the driving (re)analysis, whereas the SST is determined from a different external data source. Around the experimental site there are several lakes and fjords.

Modified SRTM data with a horizontal grid spacing of 90 m was used [Vie, 2015] for describing the terrain elevation in the WRF model.

3.2.4 Sea surface temperature

To investigate the impact of the SST on the simulations, we used two different data sources. The first product is a real-time global (RTG) daily high-resolution (HR) SST analysis from the National Centers of Environmental Prediction (NCEP). The resolution of this product is 1/12° [*Gemmill, W. and Katz, B. and Li*, 2007]. In Table 2 this SST product is abbreviated as HR.

In winter, there can be significant gradients in SST near the coast in Denmark. A product that resolves well these strong SST gradients near the coast, is the new high-resolution SST data set developed by the Danish Meteorological Institute (DMI). The Level 4 DMI North Sea-Baltic Sea daily analysis has a resolution of 0.02 degrees [*Høyer and Karagali*, 2016]. It has been specifically developed taking into consideration the conditions occurring in the Scandinavian region. These data were provided by GHRSST, DMI and the MyOcean regional data assembly centre.

The mean SST difference between the two data sources during the RUNE experimental period at positions 6 and 7 was small, but in other places it was significant; at the northern tip of Jutland, the DMI data set had a mean SST that was $\approx 2\ ^\circ$ C warmer than the HR data set. Near the south coast of Denmark there were areas where the DMI data set had a SST that was $\approx 1\ ^\circ$ C colder than those from the HR data set.

3.2.5 Driving global analysis

The atmospheric initial and boundary conditions that drive the mesoscale model can greatly influence the mean wind speed and model skill [*Floors et al.*, 2013]. Therefore, data from the Final Analysis (FNL) from the NCEP [*National Centers for Environmental Prediction, National Weather Service, NOAA*, 2015] and the ERA Interim Reanalysis from the European Centre for Medium-Range Weather Forecasts [*Dee et al.*, 2011] were used here.

Initially all simulations were performed with the FNL data, because these were available near real-time. All simulations were performed with a delay of ≈ 2 days. The ERA interim data are available with a delay of ≈ 2 months. Because more observations have been assimilated in this data set compared to FNL, it is more likely to represent most closely the atmospheric conditions during the campaign. The horizontal grid spacing of the FNL data is 0.25°, whereas it is 0.75° for the ERA interim data.

4 Results

4.1 Vertical profiles

The mean wind speed from the vertically profiling lidars and those simulated by WRF using the MYJ scheme are shown in Fig. 4. For each panel the observations from the lidar and the model were merged for each available time stamp, so that they are concurrent. At location 2 (at the coast), there are available measurements from both a short and a long-range lidar. It can be seen that all model simulations underestimate the mean wind speed at all heights. Near the surface the bias is largest and $\approx -0.7\ \mathrm{m\,s^{-1}}$ using the $\mathrm{MYJ}_{0.5}$ simulation. The mean wind speed near the ground is high due to the lidar position close to sea, where the wind speed is likely influenced by an orographic speed-up resulting from the cliff.

At location 4, i.e. ≈ 1 km inland, the mean wind speed near the ground has decreased due to the effect of local topography. All model simulations represent the mean wind speed

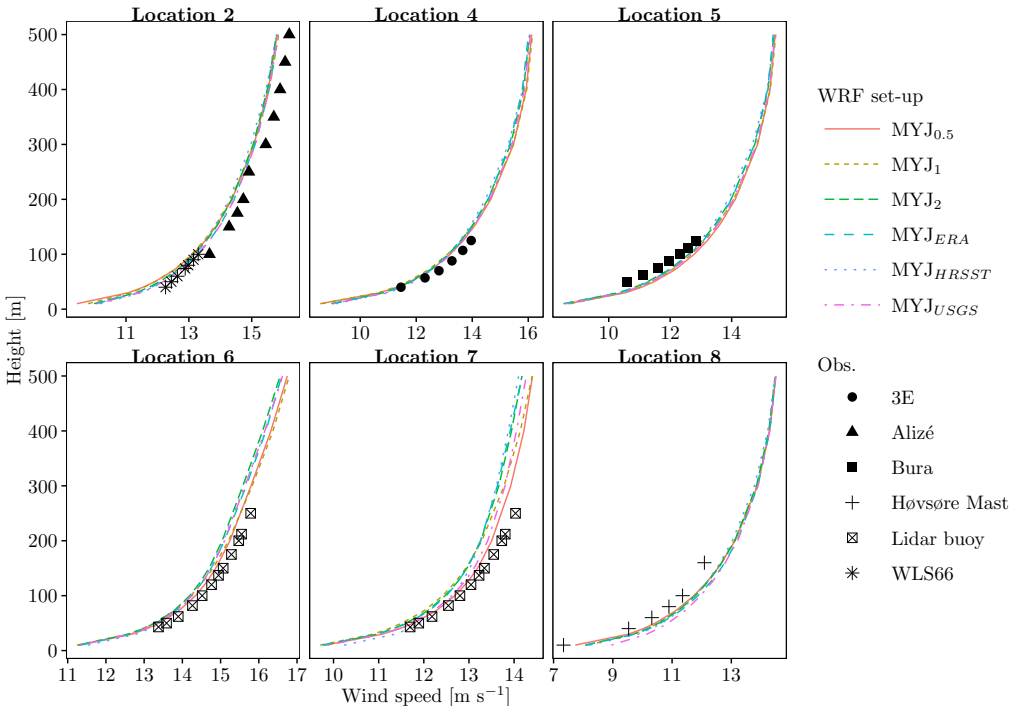

297 **Figure 4.** The mean simulated and observed wind speed ($m\,s^{-1}$) as a function of height (10–500 m) during
298 the RUNE campaign using the simulations with the MYJ PBL scheme (Table 2) at different locations (Table
299 1). The number of available 10-min intervals for each panel is shown in Table 1.

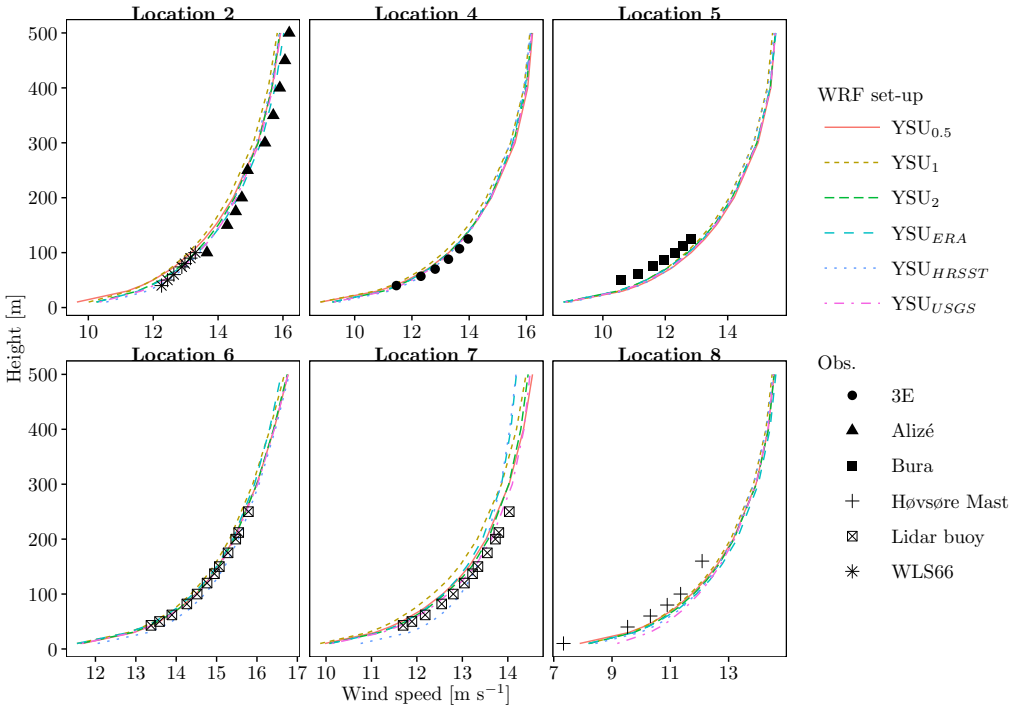

Figure 5. As in Fig. 4, but with the YSU PBL scheme.

at this location quite well, despite an slight underestimation at all heights. At location 5, i.e. $\approx$ 1.5 km inland, all model simulations slightly overestimate the mean wind speed.

Offshore, at locations 6 and 7, the mean wind speed is much higher than over land. Larger differences are visible between the different model simulations, partly because of the short observation period. At all heights the simulated mean wind speed is lower than that observed. The MYJ$_{0.5}$ simulation has the highest mean wind speed at 500 m, whereas the MYJ$_{\text{HRSST}}$ simulation shows the highest mean wind speed near the surface.

Location 8 (meteorological mast) is the most inland location and identified from the low mean wind speeds. Here the MYJ$_{\text{USGS}}$ simulation has a much higher wind speed near the surface than the other simulations, which is a consequence of the reduced surface roughness in the simulation using the USGS land use (see Fig. 1, panel b). At 500 m above the surface, the differences in mean wind speed between the different simulations are negligible.

All the simulations that used the YSU PBL scheme are shown in Fig. 4. Generally the results are very similar as when the MYJ scheme is used (Fig. 4), except at the two offshore locations 6 and 7. Here, all simulations with the YSU scheme have a smaller bias than those

using the MYJ scheme. The difference in mean wind speed between the model simulations and the observations is very small ($\lesssim 0.1 \mathrm{m\,s^{-1}}$) at location 6.

4.2 Cross sections

In this section we evaluate the mean wind speed across the experimental site from 5 km offshore up to 2 km inland. We required that all sampling points fulfilled the quality criteria that are discussed in Sect 2.2. Furthermore, we required availability of the vertically profiling lidars during the same period, to be able to compare the two data sources. Finally, we can compare the sector scan that has some sampling points at the same locations as the the dual setup. An all-sector mean wind speed at all the dual-setup locations using the 731 10-min periods at at 50, 100 and 150 m amsl that remained after filtering are shown in Fig. 6. The model output from all simulations was extracted during the same 10-min intervals.

At 50 m amsl and at 5 km offshore, the mean simulated wind speed is slightly higher than that observed with the dual setup. The sector scan shows a mean wind speed that is $\approx 0.3\ \mathrm{m\,s^{-1}}$ higher than that of the dual-setup mainly due to the problems of accurately reconstructing a wind speed when the wind is perpendicular to the line-of-sight [*Floors et al.*, 2016]. Near the coast this problem is less pronounced due to the shorter arc-length and the mean wind speed from the dual and sector scan setup agree well.

East of the coastline the observed mean wind speed from the dual setup at 50 m amsl is significantly lower than that simulated. This is likely because the flow in the mesoscale model needs a few grid points to adjust to the new logarithmic wind profile that results from the higher surface roughness. Furthermore, the real terrain height is higher than that in the simulations, which causes the wind speeds obtained from the dual setup to be closer to the surface. This is because the measurements and simulations could only be compared at a height relative to sea level and not to the surface (see Sect. 2.2). The effect of horizontal resolution is visible by the strong decrease in wind speed near the coastline of the simulations with highest horizontal resolution, $\mathrm{YSU}_{0.5}$ and $\mathrm{MYJ}_{0.5}$, that can better resolve the fast deceleration of the flow. Moving towards the land from an offshore position closer to the coastline, the mean wind speed from the dual-setup decreases more than that from the model simulations. This is probably due to flow blocking effect of the cliff, which is not represented in the WRF model simulations.

At the furthest offshore position reached by the dual setup at 50 m amsl, the YSU_{HRSST} simulation shows the highest mean wind speed and the MYJ_{ERA} simulation the lowest. The mean wind speed from all the simulations do differ by less than 0.5 $m\,s^{-1}$, so the sensitivity of the mean wind speed gradient to the different model setups is quite low. However, most YSU simulations show a stronger decrease of the mean wind speed eastward of the coastline and higher offshore mean wind speeds compared to the MYJ simulations. A more detailed description of model performance is given in Sect. 4.3.

At 100 m amsl, all simulations over-predict the mean wind speed both offshore and onshore. The $YSU_{0.5}$ simulation shows the highest mean wind speed. Although the vertically profiling lidars do not measure the wind in the same exact position as the dual setup, the mean wind speed from the vertically profiling lidars also decreases moving from the coastline inland. The mean wind speed from 3E and Bura is lower than that from the dual setup, mainly due to the terrain height at those positions; Bura and 3E measured closer to the ground than WLS66.

At 150 m amsl the east-west gradient in mean wind speed is less pronounced than at 50 and 100 m amsl. This is due to the smaller influence of the land at these heights. Still, all model simulations over-predict (by 0.5–0.8$m\,s^{-1}$) the mean wind speed compared to the dual-setup observations.

One could argue that the strict filtering can cause the cross sections to not be representative of the mean wind conditions of the 4 month period. Thus, we also studied the mean wind speed for a shorter scanning distance offshore, such that more transects were available. Including transects that extend to no more than 2 km away from the coast (not shown) increased the data recovery percentage to 15%. The over-prediction was slightly smaller for this data set, but qualitatively it did not change the patterns described above.

Although the different model simulations show similar wind speeds here, larger differences in wind speed at 100 m were observed downstream of the coastline on a transect located further north (not shown). This is because of patches of different landuse and roughness that were unresolved in some of the 2-km and USGS simulations. This shows that the similar wind speeds of different model set-ups at this transect are partly caused by the homogeneous terrain that was selected to carry out the measurements.

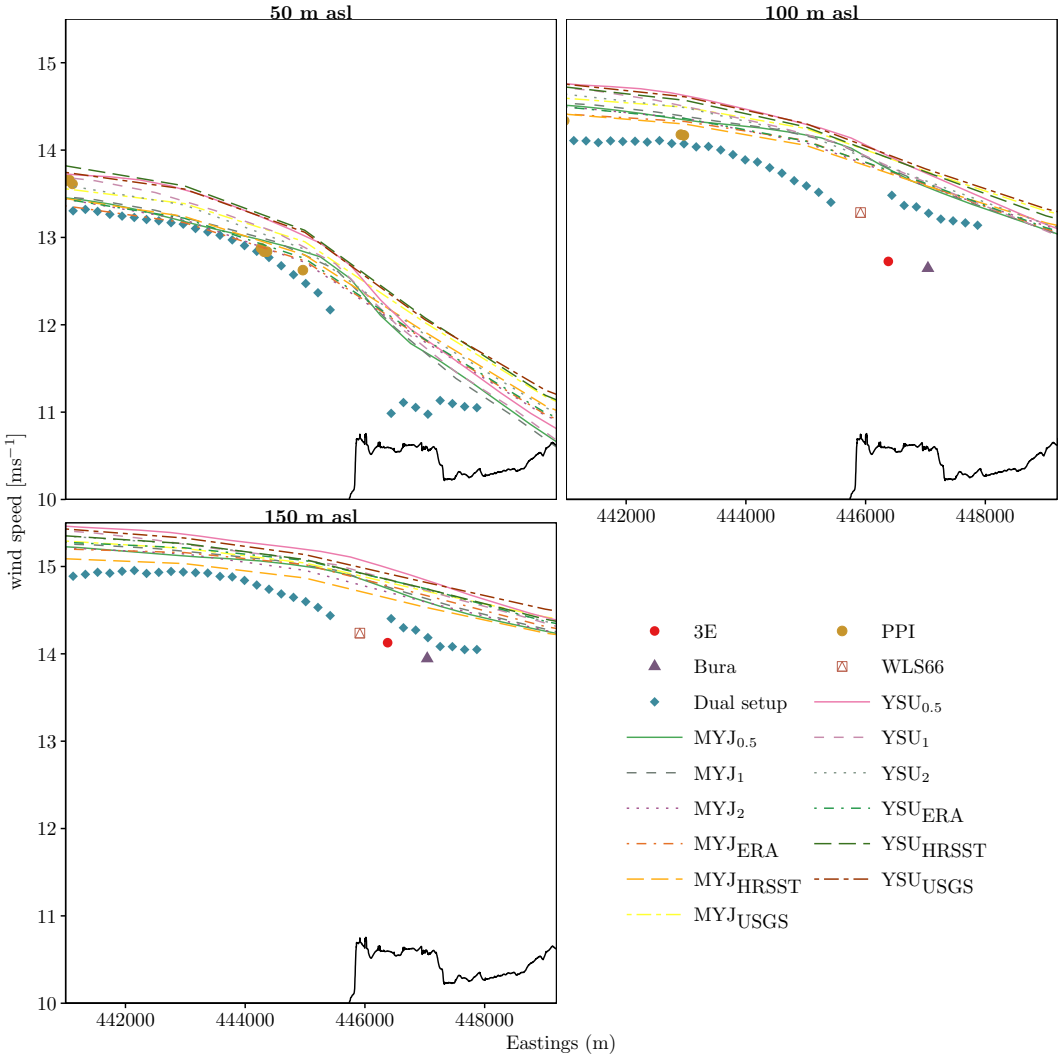

Figure 6. The reconstructed mean wind speed obtained from the sector-scan and dual setup and the vertical profiling lidars between 5000 m offshore and 2000 m inland (points) and the simulations (lines, Table 2) at three heights amsl: 50 m (top left), 100 m (top right) and 150 m (bottom left). The black lines denotes the terrain height (not to scale).

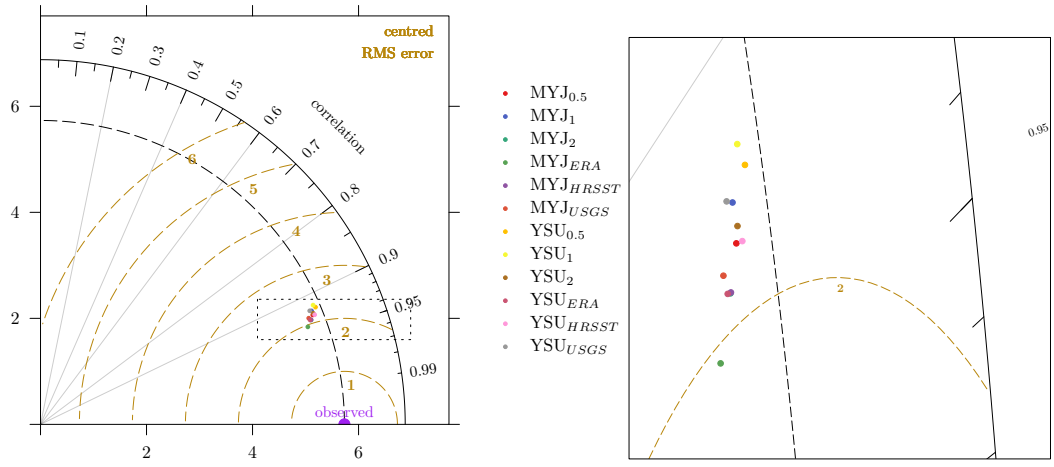

Figure 7. Taylor diagrams of the model performance of the simulated wind speed in various setups during the experiment using all 237493 10-minute intervals from all lidars in VAD mode and the meteorological mast at all available heights. The area of the plot shown in the right panel is denoted with a dashed line in the left figure.

4.3 Overall model performance

We use Taylor diagrams to evaluate the model performance in more detail [*Taylor*, 2001]. The diagrams combine the correlation coefficient (R), centered root-mean-square error (RMSE) and standard deviation (σ) of observed and modelled variables. The correlation coefficient, R, is defined as

$$R = \frac{1}{\sigma_x \sigma_y} \frac{1}{N} \sum_{i=1}^{N} (x_i - \overline{x})(y_i - \overline{y}), \tag{1}$$

where N is the number of samples, x_i is the observed variable, y_i is the modelled variable and the overbar and σ denotes their mean and standard deviation, respectively. The centered RMSE is defined as

$$\mathrm{RMSE} = \sqrt{\frac{1}{N} \sum_{i=1}^{N} [(x_i - \overline{x}) - (y_i - \overline{y})]^2}. \tag{2}$$

An example of a Taylor diagram is shown in Fig. 7. The distance from the origin denotes the standard deviation. For clarity, the standard deviation of the observations is denoted with a dashed black line. The correlation coefficient is given by the radial position on the diagram, with the x-axis denoting a correlation coefficient of 1, i.e. a perfect agreement between observations and model. Finally, the distance to the point denoting the observations is proportional to the RMSE.

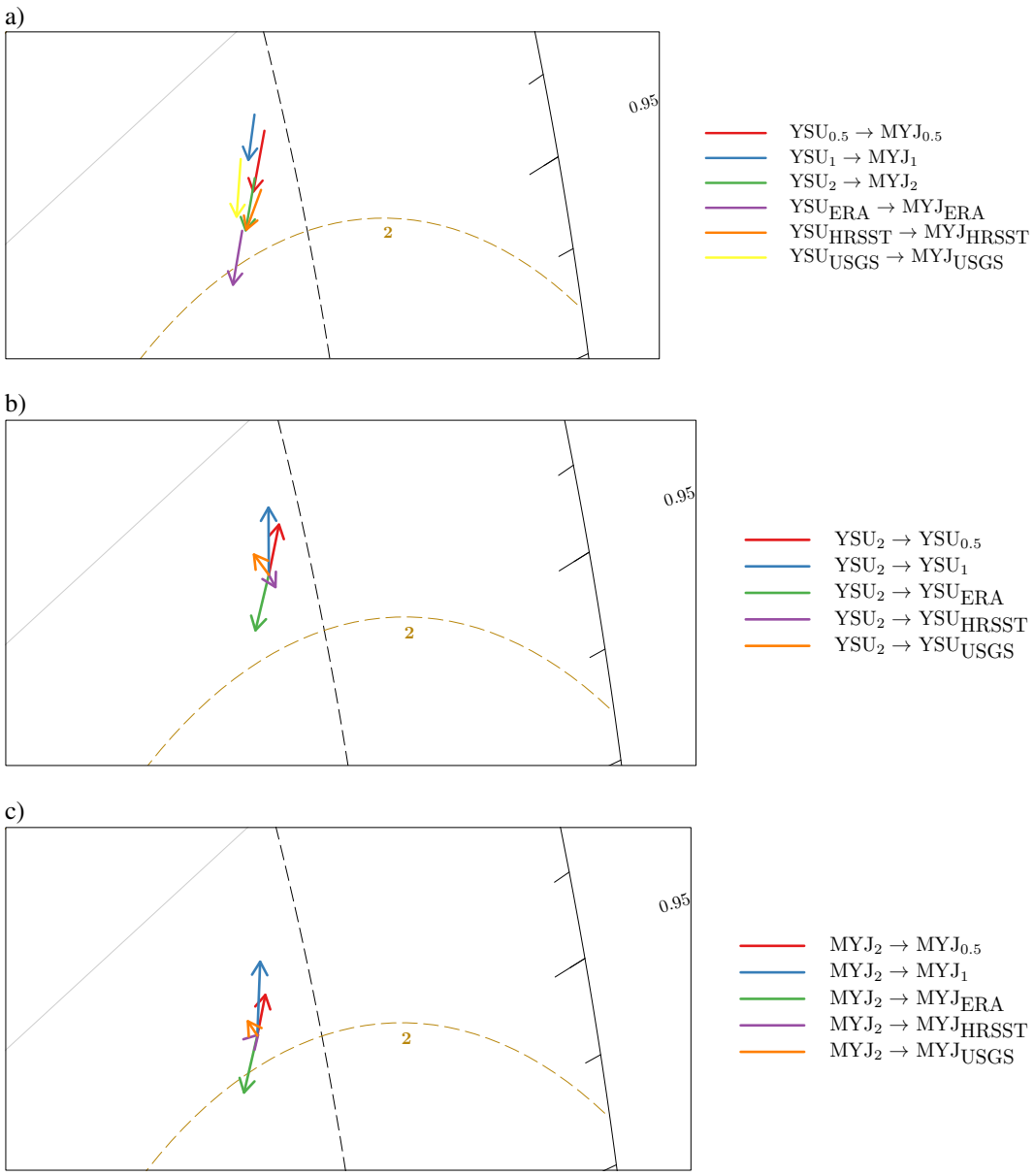

Figure 8. Taylor diagrams showing the influence to the wind speed of changing the PBL scheme from YSU to MYJ (a), the influence of changing the source of SSTs, horizontal resolution, reanalysis data and land-surface scheme for the MYJ scheme (b) and for the YSU scheme (c) and keeping the rest of the model configuration constant.

The right panel of Fig. 7 shows a zoomed view of the left Taylor diagram, to better distinguish the different model simulations. The same zoomed area is used for all the other Taylor diagrams in this section, such that we can easily compare the impact of changing a model setup.

Most of the simulations have a RMSE around 2 $\mathrm{m\,s^{-1}}$ and a standard deviation around 5.5 $\mathrm{m\,s^{-1}}$. However, a more clear overview of the impact of changing an element of the model configuration can be achieved by drawing an arrow from a 'control' simulation to a simulation with a certain change. If the arrow points downward, it indicates that the correlation coefficient has increased and the centered RMSE has decreased, i.e. a better model performance.

First we investigate the impact of changing the PBL scheme, by drawing an arrow from those simulations that use the YSU PBL scheme to the ones using the MYJ scheme. Fig. 8a shows that this change leads to a better model performance: all the arrows are pointing downward, i.e. an increased correlation coefficient and decreased centered RMSE, indicating that the MYJ scheme performs better than the YSU scheme in this period. However, all arrows are pointing away from the line with the observed wind speed standard deviation, which means that the standard deviation is lower in the model simulations with the MYJ scheme than those with the YSU scheme.

In Fig. 8b we show the impact of changing the horizontal resolution and the SST, land and atmospheric boundary conditions using the YSU PBL scheme. Using the ERA-interim instead of the FNL atmospheric boundary conditions results in an improved model performance. This is not a trivial result, because the ERA-interim data has a much lower resolution but also has more observations assimilated in it.

Increasing the horizontal grid spacing from the control 2 km results in a decreased model performance. Both the $\mathrm{YSU_1}$ and $\mathrm{YSU_{0.5}}$ show a lower correlation coefficient and higher centered RMSE compared to the $\mathrm{YSU_2}$ simulation. The simulations with higher horizontal resolution resolve more atmospheric motions and have a higher variance: this results in a higher RMSE if the correlation coefficient between the simulated and observed wind speeds is smaller than one. It is well known that standard metrics are often penalized by increased resolution [*Uttal et al.*, 2002]. This issue is further investigated in Sect. 4.4.

To investigate whether the model performance changed only in the surface layer, the diagrams were split in heights below and above 80 m above ground level. Using USGS data instead of the CORINE land cover data results in decreased model performance below 80 m and above 80 m the difference between these simulations was negligible (not shown). Using the HR compared to the DMI SST product has a very small impact on the model performance (Fig. 8c). However, it is possible that larger differences in error metrics are seen in other regions with larger differences in SST.

Fig. 8c shows the same sensitivities as 8b, but using the MYJ scheme. The impact of changing e.g. atmospheric or surface boundary conditions is very similar compared to that seen when the YSU scheme is used. This confirms the statistical robustness of the results and shows that the model responds similarly to changing the boundary conditions when different PBL schemes are used. The only exception is that the arrow from the $MYJ_{0.5}$ simulation is shorter, indicating that using a higher resolution with the MYJ scheme does not decrease the model performance as much as when using the YSU scheme. We do not understand fully the reason for this, but this issue is further investigated in Sect. 4.4).

The error metrics of all simulations are summarized in Table 3. The MYJ_{ERA} has the lowest RMSE and mean absolute error. The mean bias is not available in the Taylor diagram. From this metric the MYJ_{ERA} performs well (bias of $-0.04\ \mathrm{m\,s^{-1}}$), but the setup with the lowest overall bias is the YSU_2 simulation ($0.02\ \mathrm{m\,s^{-1}}$). There is very low mean relative errors between the simulated and observed mean wind speed, which shows that when multiple heights and locations are used for a comparison, the mesoscale model predicts the mean wind speed in this area very well. At individual sites and heights, however, there are still larger errors mostly due to terrain effects not present in the WRF model (see Fig. 4.1).

4.4 Observed and simulated velocity spectra

The model setups with a higher horizontal resolution resolve a larger range of atmospheric motions. To investigate the impact of increasing the resolution, we compare the spectra of the wind speed from the measurements and the model output from the simulations at the Høvsøre mast at 100 m. To avoid a noisy appearance in the high frequency part of the spectrum, the observed spectra were smoothed by computing an average of a maximum of 15 Fourier coefficients in each decade, whereas for the modelled spectra this number was 5. We

457 **Table 3.** Error metrics using 237493 available 10-min measurements from all heights and locations. The
458 mean absolute error is defined as $\frac{1}{N}\sum_{i=1}^{N}|y_i - x_i|$, the mean bias as $\overline{y_i} - \overline{x_i}$ and the mean relative error as
459 $100(\overline{y_i} - \overline{x_i})/\overline{x_i}$. The best performing simulation for each error metric is shown in bold.

Setup	RMSE ($m\,s^{-1}$)	Mean abs. err. ($m\,s^{-1}$)	Mean bias ($m\,s^{-1}$)	R (-)	Mean mod. ($m\,s^{-1}$)	Mean obs. ($m\,s^{-1}$)	Mean rel. err. (%)
$MYJ_{0.5}$	2.15	1.56	-0.16	0.93	12.11	12.27	-1.31
MYJ_{1}	2.23	1.61	-0.16	0.92	12.11	12.27	-1.29
MYJ_{2}	2.07	1.50	-0.10	0.93	12.17	12.27	-0.79
MYJ_{ERA}	**1.96**	**1.48**	-0.04	**0.94**	12.23	12.27	-0.31
MYJ_{HRSST}	2.07	1.51	-0.05	0.93	12.22	12.27	-0.39
MYJ_{USGS}	2.11	1.56	0.09	0.93	12.36	12.27	0.73
$YSU_{0.5}$	2.28	1.65	-0.09	0.92	12.17	12.27	-0.76
YSU_{1}	2.33	1.67	-0.16	0.92	12.11	12.27	-1.31
YSU_{2}	2.18	1.57	**0.02**	0.93	12.29	12.27	**0.15**
YSU_{ERA}	2.07	1.54	0.06	0.93	12.33	12.27	0.47
YSU_{HRSST}	2.14	1.54	0.14	0.93	12.41	12.27	1.14
YSU_{USGS}	2.24	1.64	0.20	0.92	12.47	12.27	1.61

also extracted the modelled time series from the second domain of configuration $MYJ_{3.0}$ and $YSU_{3.0}$ to compare more horizontal grid spacings.

Larsén et al. [2016] discussed the different frequency (f) ranges of atmospheric spectra: at lower frequencies between 1 year^{-1} < f < 1 day^{-1} the slope of the power spectra, $S(f)$, versus f in the log-log scale is ≈ -3, between 1 day^{-1} < f < 1 hour^{-1} it is $\approx -5/3$ and at higher frequencies the uncertainty in slope is rather high and depends on the existence of a spectral gap that separates mesoscale and turbulent motions.

In Fig. 9 (top) the MYJ scheme matches well the observed spectra at frequencies larger than 1 day^{-1}. Between frequencies of 1 day^{-1} and 1 hour^{-1}, all model simulations gradually start to under-predict the spectral density. This is caused by the numerical filters that are applied in a mesoscale model [*Skamarock*, 2004] to keep a stable model solution. When f < 1 hour^{-1} there are distinct differences between the simulation results from different horizontal grid spacings: the $MYJ_{0.5}$ and $MYJ_{1.0}$ simulations have a much higher spectral density than the other coarser resolutions. The $MYJ_{3.0}$ simulation shows a rather steep decline when f < 1 hour^{-1}, showing that it does not resolve these motions with this grid spacing. Therefore, a 10-minute output frequency with a grid of 3 km spacing is unnecessary.

The simulations $MYJ_{0.5}$ and $MYJ_{1.0}$ have a rather different spectral slope when f < 1 hour^{-1} compared to the simulations with higher horizontal grid spacing. *Skamarock* [2004] argued that such an upward turned tail in the high frequencies indicates a model that has an non-physical treatment of these atmospheric motions. On the other hand, the observed spectral slope is similar to the modelled one for the simulations $MYJ_{1.0}$ and $MYJ_{1.5}$ and for these grid spacings it is possible that the model is capable to better represent high-frequency motions due to the higher resolution.

Note that the simulations with a grid spacing of 1 km have a higher spectral energy at high frequencies than those with 0.5 km spacing. This is likely due to the model configuration in the outer domains; the $MYJ_{0.5}$ has a higher resolution near the site, but the 4th domain only covers a small area (see Fig. 3). In domains 2 and 3, MYJ_1 has a higher resolution than $MYJ_{0.5}$.

The velocity spectra from the simulations using the YSU scheme are shown in Fig. 9 (bottom). In general, simulations with the YSU scheme have higher spectral energy than those with the MYJ scheme. Particularly the $YSU_{0.5}$ simulation has a higher spectral energy

than the observations at high frequencies. This could indicate that these high-resolution simulations do not realistically model high-frequency atmospheric fluctuations.

Honnert et al. [2011] noted that mesoscale models with 'terra incognita' resolutions produce too many resolved fluctuations in a convective boundary layer. *Zhou et al.* [2014] used the Rayleigh-Benard thermal instability theory and a set of idealized simulations to explain the occurrence of this higher variance. Here, the simulations with the finest horizontal grid spacing can be influenced by such modelling issues and this could also possibly explain the higher spectral energy at high frequencies.

Finally, it was found that the velocity spectra were not influenced by the choice of grid point. This was investigated by comparing the modelled spectra ≈ 10 km offshore with those inland near the Høvsøre mast; the velocity spectra at both locations were very similar.

The velocity spectra also partially explain the higher RMSE between model and observations of the simulations $\mathrm{YSU}_{0.5}$ and $\mathrm{MYJ}_{0.5}$. These simulations also have a higher standard deviation (see Fig. 7) than the simulations with lower resolution. Therefore investigation of velocity spectra of mesoscale model set-ups gives an idea of the model representation of motions in the different scales.

5 Summary and discussion

A number of mesoscale model simulations was performed to test the sensitivity of the simulated wind in the PBL to use different PBL schemes, atmospheric forcing, SST descriptions, land use descriptions and horizontal grid spacing for a site along the Danish west coast. The model results were compared with observations from five vertical profiling lidars and scanning lidars at multiple heights and locations.

All mesoscale model setups were able to simulate well the mean vertical profile at different locations and the decrease of mean wind speed when moving inland was similar as observed, despite the relatively coarse resolution of some of the model simulations. The mean wind speed differences among the different setups were very small, although this is partially because of the homogeneous terrain at the experimental site. The YSU scheme had a smaller bias than the MYJ scheme at the offshore positions. This indicates that mesoscale models can estimate the mean vertical wind shear at the hub height of wind turbines well, even in the complex coastal zone.

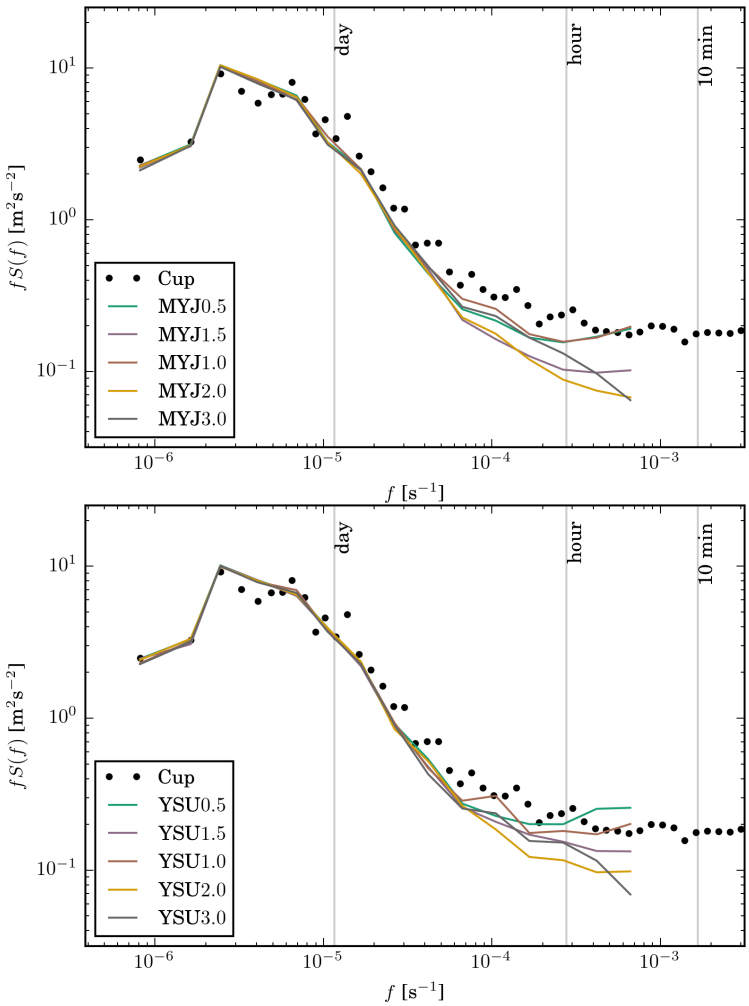

514 **Figure 9.** Velocity spectra of the model simulations at the Høvsøre mast at 100 m with different horizontal
515 resolutions using the MYJ (top) and the YSU scheme (bottom) compared to those of the observations from the
516 cup anemometer.

Due to the availability of scanning lidar measurements, we were for the first time able to spatially evaluate the mean horizontal wind speed gradient simulated by the mesoscale model setups. The observed mean wind speed was $\approx$0.5 m s^{-1} lower than that simulated at the furthest offshore position; however the amount of samples is low. Moving inland from the coast, the mesoscale model did not represent the strong decrease in mean wind speed at 50 m well, probably because the microscale features of the terrain are not well resolved, both in the prescribed initial conditions and in the model itself. Increasing the horizontal resolution of the simulations did not result in a better representation of the horizontal gradient of mean wind speed.

Despite the small differences in mean wind speed among the different simulations, using Taylor diagrams revealed that there were still differences in other error metrics. Using the MYJ instead of the YSU scheme, caused lower RMSEs and higher correlation coefficients in combination with all model setups. Simulating the flow using ERA interim boundary conditions also led to better model predictions compared to those using FNL data. Using a horizontal grid spacing of 0.5 or 1 instead of 2 km resulted in a higher RMSE and lower correlation coefficient, showing that a finer resolution forecast is not always more skillful. Using CORINE instead of USGS land cover description improved the model skill near the surface, but did not have a substantial influence higher up. Using the HR compared to the DMI SSTs only had a minor impact on the model skill.

The velocity spectra from the simulations were compared to those obtained from the high frequency cup anemometer data. The observed and modelled spectra agreed well at the low-frequencies ($f \approx 1$ day$^{-}1$), but there were large differences between the simulations with different horizontal grid spacings at high frequencies ($f \approx 1$ hour$^{-}1$). All simulations contained less spectral energy than the observations at frequencies of ≈ 1 hour^{-1}. For the simulations with 0.5 km grid spacing, the tail of the spectra turned upwards at high frequencies. This indicates that care should be taken (e.g. by using appropriate parametrization and diffusion constants) when high horizontal resolutions are used in a mesoscale model. Here, the much larger computational costs of using 0.5–1 compared to 2 km grid spacing were not needed to accurately simulate the flow in the coastal zone using the WRF model.

Acknowledgments

Funding from the ForskEL program to the project ‘RUNE’ No. 12263 and The European Commission and the Energiteknologiske Udviklings- og Demonstrationsprogram (EUDP)

563 funded ‘New European Wind Atlas’ project through FP7 are acknowledged. We would also
564 like to acknowledge 3E for adding the 3E lidar to RUNE’s network, Fraunhofer IWES for
565 the measurements from the lidar buoy, and the technicians of DTU Wind Energy, Fraunhofer
566 IWES and the Danish Hydrological Institute for their work and support during the campaign.
567 The data used in this paper are available for download [*Floors et al.*, 2017].

568 **References**

569 (2006), CORINE landcover data http://www.eea.europa.eu/data-and-maps/data/CORINE-
570 land-cover-2006-raster-3#tab-metadata.

571 (2015), WRF 3.6 Patches http://www2.mmm.ucar.edu/wrf/users/wrfv3.6/known-prob-
572 3.6.html.

573 (2015), SRTM data http://www.viewfinderpanoramas.org/dem3.html.

574 Anderson, J. R., E. E. Harde, J. T. Roach, and R. E. Witmer (1976), *A land use and land*
575 *cover classification system for use with remote sensor data*, vol. 964, vol. 964 ed., 27 pp.,
576 US Government Printing Office, Washington, USA.

577 Barthelmie, R., J. Badger, S. Pryor, C. Hasager, M. Christiansen, and B. Jørgensen (2007),
578 Offshore Coastal Wind Speed Gradients: issues for the design and development of large
579 offshore windfarms, *Wind Eng.*, *31*(6), 369–382, doi:10.1260/030952407784079762.

580 Dee, D. P., S. M. Uppala, A. J. Simmons, P. Berrisford, P. Poli, S. Kobayashi, U. Andrae,
581 M. a. Balmaseda, G. Balsamo, P. Bauer, P. Bechtold, a. C. M. Beljaars, L. van de Berg,
582 J. Bidlot, N. Bormann, C. Delsol, R. Dragani, M. Fuentes, a. J. Geer, L. Haimberger,
583 S. B. Healy, H. Hersbach, E. V. Hólm, L. Isaksen, P. Kållberg, M. Köhler, M. Matricardi,
584 a. P. McNally, B. M. Monge-Sanz, J.-J. Morcrette, B.-K. Park, C. Peubey, P. de Rosnay,
585 C. Tavolato, J.-N. Thépaut, and F. Vitart (2011), The ERA-Interim reanalysis: configura-
586 tion and performance of the data assimilation system, *Q. J. R. Meteorol. Soc.*, *137*(656),
587 553–597, doi:10.1002/qj.828.

588 Dörenkämper, M., M. Optis, A. Monahan, and G. Steinfeld (2015), On the Offshore Ad-
589 vection of Boundary-Layer Structures and the Influence on Offshore Wind Conditions,
590 *Boundary-Layer Meteorol.*, *155*(3), 459–482, doi:10.1007/s10546-015-0008-x.

591 Dvorak, M. J., C. L. Archer, and M. Z. Jacobson (2009), California offshore wind energy
592 potential, *Renew. Energy*, *35*, 1244–1254, doi:10.1016/j.renene.2009.11.022.

593 Floors, R., C. L. Vincent, S.-E. Gryning, A. Peña, and E. Batchvarova (2013), The Wind Pro-
594 file in the Coastal Boundary Layer: Wind Lidar Measurements and Numerical Modelling,

Boundary-Layer Meteorol., *147*(3), 469–491, doi:10.1007/s10546-012-9791-9.

Floors, R., A. Peña, G. Lea, N. Vasiljević, E. Simon, and M. Courtney (2016), The RUNE Experiment—A Database of Remote-Sensing Observations of Near-Shore Winds, *Remote Sens.*, *8*(11), 884, doi:10.3390/rs8110884.

Floors, R., A. N. Hahmann, and A. Peña (2017), Files with RUNE experiment measurements and WRF modelling results, doi:10.5281/ZENODO.834635.

Frank, H. P., O. Rathmann, N. G. Mortensen, and L. Landberg (2001), The numerical wind atlas - the KAMM/WAsP method.

Gemmill, W. and Katz, B. and Li, X. (2007), Daily real-time global sea surface temperature—High resolution analysis at NOAA/NCEP, *Tech. rep.*, NCEP/NOAA.

Gryning, S.-E., R. Floors, A. Peña, E. Batchvarova, and B. Brümmer (2016), Weibull Wind-Speed Distribution Parameters Derived from a Combination of Wind-Lidar and Tall-Mast Measurements Over Land, Coastal and Marine Sites, *Boundary-Layer Meteorol.*, *159*(2), 329–348, doi:10.1007/s10546-015-0113-x.

Hahmann, A. N., C. L. Vincent, A. Peña, J. Lange, and C. B. Hasager (2015), Wind climate estimation using WRF model output: method and model sensitivities over the sea, *Int. J. Climatol.*, *35*(12), 3422–3439, doi:10.1002/joc.4217.

Honnert, R., V. Masson, and F. Couvreux (2011), A Diagnostic for Evaluating the Representation of Turbulence in Atmospheric Models at the Kilometric Scale, *J. Atmos. Sci.*, *68*(12), 3112–3131, doi:10.1175/JAS-D-11-061.1.

Høyer, J. L., and I. Karagali (2016), Sea Surface Temperature Climate Data Record for the North Sea and Baltic Sea, *J. Clim.*, *29*(7), 2529–2541, doi:10.1175/JCLI-D-15-0663.1.

Hunt, J., A. Orr, J. Rottman, and R. Capon (2004), Coriolis effects in mesoscale flows with sharp changes in surface conditions, *Q. J. R. Meteorol. Soc.*, *130*(603), 2703–2731, doi:10.1256/qj.04.14.

Janjić, Z. I. (1990), The Step-Mountain Coordinate: Physical Package, *Mon. Weather Rev.*, *118*(7), 1429–1443, doi:10.1175/1520-0493(1990)118<1429:TSMCPP>2.0.CO;2.

Lange, B., S. Larsen, J. Højstrup, and R. Barthelmie (2004), Importance of thermal effects and sea surface roughness for offshore wind resource assessment, *J. Wind Eng. Ind. Aerodyn.*, *92*(11), 959–988, doi:10.1016/j.jweia.2004.05.005.

Larsén, X. G., S. E. Larsen, and E. L. Petersen (2016), Full-Scale Spectrum of Boundary-Layer Winds, *Boundary-Layer Meteorol.*, *159*(2), 349–371, doi:10.1007/s10546-016-0129-x.

Mikkelsen, T. (2014), Lidar-based Research and Innovation at DTU Wind Energy – a Review, *J. Phys. Conf. Ser.*, *524*(1), 012,007, doi:10.1088/1742-6596/524/1/012007.

National Centers for Environmental Prediction, National Weather Service, NOAA, U. D. o. C. (2015), NCEP GDAS/FNL 0.25 Degree Global Tropospheric Analyses and Forecast Grids, doi:10.5065/D65Q4T4Z.

Nielsen, J. R. (2013), Representing vegetation processes in hydro-meteorological simulations using the WRF model, Phd thesis, Risø-PhD-0016(EN), Risø National Laboratory for Sustainable Energy, Technical University of Denmark, Roskilde, Denmark, 128 pp.

Noh, Y., W. G. Cheon, and S. Y. Hong (2003), Improvement of the K-profile Model for the Planetary Boundary Layer based on Large Eddy Simulation Data, *Boundary-Layer Meteorol.*, *107*(2), 401–427, doi:10.1023/A:1022146015946.

Olsen, B. T., A. N. Hahmann, A. M. Sempreviva, J. Badger, and H. E. Jørgensen (2017), An intercomparison of mesoscale models at simple sites for wind energy applications, *Wind Energy Sci.*, *2*(1), 211–228, doi:10.5194/wes-2-211-2017.

Peña, A., R. Floors, A. Sathe, S.-E. Gryning, R. Wagner, M. S. Courtney, X. G. Larsén, A. N. Hahmann, and C. B. Hasager (2016), Ten Years of Boundary-Layer and Wind-Power Meteorology at Høvsøre, Denmark, *Boundary-Layer Meteorol.*, *158*(1), 1–26, doi:10.1007/s10546-015-0079-8.

Pindea, N., O. Jorba, J. Jorge, and Baldasano (2002), Using NOAA-AVHRR and SPOT-VGT data to estimate surface parameters : application to a mesoscale meteorological model, *1st Int. Symp. Recent Adv. Quant. Remote Sens.*, *1161*(June), 16–20, doi:10.1080/0143116031000115201.

Shin, H. H., and J. Dudhia (2016), Evaluation of PBL Parameterizations in WRF at Subkilometer Grid Spacings: Turbulence Statistics in the Dry Convective Boundary Layer, *Mon. Weather Rev.*, *144*(3), 1161–1177, doi:10.1175/MWR-D-15-0208.1.

Skamarock, W. C. (2004), Evaluating Mesoscale NWP Models Using Kinetic Energy Spectra, *Mon. Weather Rev.*, *132*(12), 3019–3032, doi:10.1175/MWR2830.1.

Skamarock, W. C., J. B. Klemp, J. Dudhia, D. O. Gill, D. M. Barker, M. G. Duda, X.-Y. Huang, W. Wang, and J. G. Powers (2008), A description of the Advanced Research WRF version 3, *Tech. rep.*, NCAR/TN-475+ STR, 113 pp. Mesoscale and Microscale Meteorology Division, National Center for Atmospheric Research, Boulder.

Tammelin, B., T. Vihma, E. Atlaskin, J. Badger, C. Fortelius, H. Gregow, M. Horttanainen, J. Kilpinen, J. Latikka, K. Ljungberg, N. G. Mortensen, K. Ruosteenoja, K. Salonen,

I. Suomi, R. Hyvönen, S. Niemelä, and A. Venäläinen (2013), Production of the Finnish Wind Atlas, *Wind Energy*, *16*(1), 19–35, doi:10.1002/we.517.

Taylor, K. E. (2001), Summarizing multiple aspects of model performance in a single diagram, *J. Geophys. Res. Atmos.*, *106*(D7), 7183–7192, doi:10.1029/2000JD900719.

Uttal, T., J. A. Curry, M. G. Mcphee, D. K. Perovich, R. E. Moritz, J. A. Maslanik, P. S. Guest, H. L. Stern, J. A. Moore, R. Turenne, A. Heiberg, M. C. Serreze, D. P. Wylie, O. G. Persson, C. A. Paulson, C. Halle, J. H. Morison, P. A. Wheeler, A. Makshtas, H. Welch, M. D. Shupe, J. M. Intrieri, K. Stamnes, R. W. Lindsey, R. Pinkel, W. S. Pegau, T. P. Stanton, and T. C. Grenfeld (2002), Surface Heat Budget of the Arctic Ocean, *Bull. Am. Meteorol. Soc.*, *83*(2), 255–275, doi:10.1175/1520-0477(2002)0832.3.CO;2.

Vasiljević, N., G. Lea, M. Courtney, J.-P. Cariou, J. Mann, and T. Mikkelsen (2016), Long-Range WindScanner System, *Remote Sens.*, *8*(12), 896, doi:10.3390/rs8110896.

Wijnant, I. L., H. Van Den Brink, and A. Stepek (2014), North Sea Wind Climatology Part 2 : ERA-Interim and Harmonie model data, *Tech. rep.*, KNMI, De Bilt.

Wyngaard, J. C. (2004), Toward Numerical Modeling in the "Terra Incognita", *J. Atmos. Sci.*, *61*(14), 1816–1826, doi:10.1175/1520-0469(2004)061<1816:TNMITT>2.0.CO;2.

Zhou, B., J. S. Simon, F. K. Chow, B. Zhou, J. S. Simon, and F. K. Chow (2014), The Convective Boundary Layer in the Terra Incognita, *J. Atmos. Sci.*, *71*(7), 2545–2563, doi:10.1175/JAS-D-13-0356.1.